BULLETIN OF THE POLISH ACADEMY OF SCIENCES
TECHNICAL SCIENCES, Vol. 74(5), 2026, Article number: 1146
DOI: 10.24425/bpasts.2026.1146

Intelligent modeling and optimization of the liquid CO_2-MQL burnishing operation for friction and environmental emission

Huu-Toan BUI[1], Tung-Manh DO[1], An-Le VAN[2], and Trung-Thanh NGUYEN[1]*

[1] Faculty of Mechanical Engineering, Le Quy Don Technical University, Hanoi, Viet Nam
[2] Faculty of Engineering and Technology, Nguyen Tat Thanh University, Ho Chi Minh City, Vietnam

Abstract. In this study, a novel liquid CO_2-MQL burnishing (LCMB) process is introduced to simultaneously improve tribological and environmental outcomes during the machining of AISI H13 steel. The process considers key input parameters, including pressure of the compressed air (P), the oil flow rate (L), and the CO_2 flow rate (C), while the outputs are the coefficient of friction (COF), the maximum wear depth (WD), the $PM10$, and the vibrational amplitude along the X-axis (VX). An advanced modeling-optimization framework is employed, combining a Bayesian-tuned support vector machine (OSVM) with entropy-based weighting to characterize the responses, followed by a multi-objective grasshopper optimization algorithm (MOGOA) to generate candidate solutions. The weighted aggregated sum product assessment (WASPAS) is utilized to find the proper solution. The results demonstrated that the COF, WD, $PM10$, and VX were decreased by 5.9%, 3.5%, 22.3%, and 10.4%, respectively, as compared to user-defined values. The developed burnishing process significantly enhanced subsurface integrity by producing a deeper and more uniform plastically deformed layer compared to MQL and dry conditions, which directly contributes to improved hardness, wear resistance, and tribological performances.

Keywords: burnishing process; coefficient of friction; wear depth; vibration; MOGOA.

1. INTRODUCTION

Burnishing is an efficient surface finishing process widely used to improve surface quality, hardness, residual stress, and wear resistance through controlled plastic deformation of surface asperities. Owing to its advantages in enhancing functional performance without material removal, burnishing has been increasingly applied in precision manufacturing industries.

Several optimization techniques have been used to optimize different burnishing operations. The surface roughness, microhardness, and circularity of the burnished Mg-SiC metal matrix were enhanced using the Taguchi method [1]. The authors stated that the optimal spindle speed, feed rate, force, and the number of passes were 171 rpm, 0.18 mm/rev, 21 N, and 3, respectively. The impacts of the spindle speed, feed rate, penetration depth, and number of rollers on the surface roughness, surface hardness, and residual stress of the burnished AA6061-T6 were explored [2]. The results revealed that the roughness and hardness were primarily affected by the feed rate and depth of penetration, respectively. The ideal parameters for the burnishing E52100 steel were found using the RSM and bee colony algorithm [3]. The authors stated that roughness and hardness were improved by 76.3% and 47.7%, respectively. Hamadache *et al.* presented that the roughness, hardness, and wear resistance of the burnished CX38 were enhanced by 89.3%, 48.5%, and 42.4%, respectively, under the impacts of ball burnishing operation [4]. The optimal parameters were chosen to decrease the wear rate of the burnished Ti-6Al-4V and enhance the micro-hardness and depth of the impacted layer [5]. The results showed that 200 m/min, 0.3 mm, and 5.0 mm were the optimal burnishing speed, depth of penetration, and tool radius, respectively. Rotella *et al.* reported that applying MQL can significantly improve the surface finish of burnished Ti6Al4V, leading to lower roughness values [6]. The optimal factors of the burnishing crankshaft operation were selected using RSM [7]. The results indicated that the optimal spindle speed, number of passes, and force were 50 rpm, 10, and 23 000 N, respectively. The roughness and hardness of the burnished 36CrNiMo4 steel were enhanced using the TOPSIS [8]. The authors stated that the optimal spindle speed, feed rate, and force were 900 rpm, 0.04 mm/rev, and 120 N, respectively. For 17-4 stainless steel, the LN_2-assisted burnishing process resulted in improvements of 36.8% in surface roughness and 42.6% in Vickers hardness (VH) compared with the untreated condition [9]. Başsoy and Çelik presented that the roughness and hardness of the printed AlSi10Mg component were improved by 81.2% and 42.4%, respectively, with the aid of the ball burnishing process [10]. In addition, Maximov reported that LN_2-assisted burnishing of SS304 significantly improved fatigue strength and compressive residual stress by 35.2% and 242.8%, respectively, compared to untreated samples [11]. Furthermore, Sachin *et al.* found that using the smallest tool size increased the hardness of processed

*e-mail: trungthanhnguyen@lqdtu.edu.vn

Manuscript submitted 2026-03-19, revised 2026-05-05, initially accepted for publication 2026-05-20, published in September 2026.

© 2026 The Author(s). This is an open access article under the CC BY license (http://creativecommons.org/licenses/by/4.0/)

17-4 PH steel by approximately 4% [12]. Nevertheless, there are several limitations in the existing literature. First, the effects of cooling-related parameters on *COF*, *WD*, *PM*10, and *VX* have not been systematically investigated. Second, there are no predictive models linking these responses to cooling parameters. Third, no comprehensive optimization has been conducted to determine cooling conditions that simultaneously minimize responses.

2. OPTIMIZATION APPROACH

The *COF* is computed as:

$$COF = \frac{\sum_{i}^{n} COF_i}{n}, \tag{1}$$

where COF_i denotes the coefficient of friction at the i-th location.

The $PM10$ is computed as:

$$PM10 = \frac{\sum_{i}^{n} PM10_i}{n}, \tag{2}$$

where $PM10_i$ is the $PM10$ at the i-th time.

The *VX* is computed as:

$$VX = \frac{\sum_{i}^{n} VX_i}{n}, \tag{3}$$

where VX_i is the vibrational amplitude in the X axis at the measured time.

The *WD* value is selected at the end of the measurement process.

Three primary operating variables – *P*, *L*, and *C* – along with their corresponding ranges, are summarized in Table 1. The values of *P* and *L* are selected based on the guidelines provided for the MQL system, whereas the value of *C* is defined according to the specifications in the liquid tank user manual.

Table 1
The cooling parameters to be optimized

No.	Symbol	Parameters	Levels	Unit
1	*P*	The pressure of compressed air	0.2-0.4-0.6	MPa
2	*L*	The oil flow rate	100-150-200	ml/h
3	*C*	The flow rate of CO_2	15-20-25	L/min

The optimization approach for the LCMB process is shown in Fig. 1:

Step 1: Performing LCMB trials with 27 experiments using the Box-Behnken design [13–16].

Step 2: The entropy method is used to compute the weight of each response.

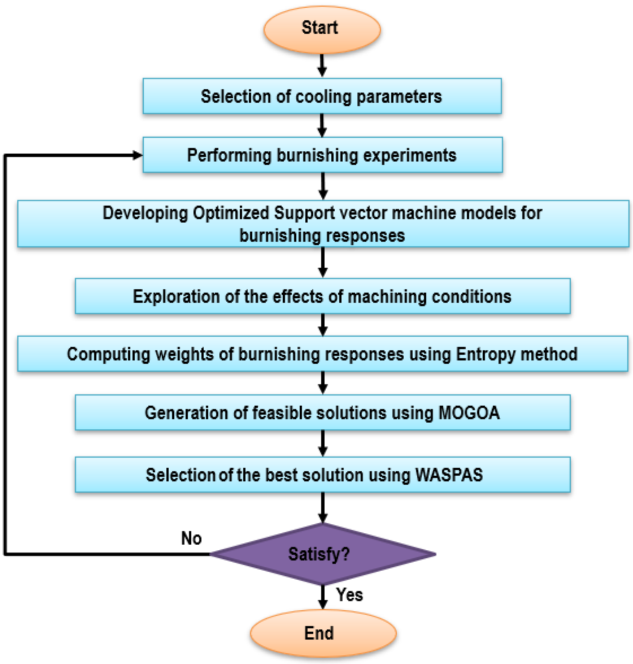

Fig. 1. The optimization approach for the LCMB process

The normalized response (p_{ij}) is calculated as:

$$p_{ij} = \frac{r_{ij}}{\sum_{i=1}^{m} r_{ij}} \quad (i = 1,\ldots,m;\ \ j = 1,\ldots,n). \tag{4}$$

The weight (ω_j) is computed as:

$$\omega_j = \frac{g_j}{\sum_{j=1}^{n} g_j}, \tag{5}$$

where g_j is the variation coefficient.

Step 3: The SVM is utilized to propose the LCMB models [17–19]. The SVM using a radial basis function kernel is expressed as:

$$f(a) = \omega.H(a,a_i) + d, \tag{6}$$

$$H(a,a_i) = \exp(? - \frac{a-a_i}{2\gamma^2}), \tag{7}$$

where $H(a,a_i)$ and γ are the kernel function and its parameter. To obtain better SVM performance, its hyperparameters, including the kernel scale (K) and epsilon (ε) need to be carefully tuned and optimized [20,21]. The indicators, including the mean squared error (MSE) and the mean absolute error (MAE) are used to evaluate the adequacy of models [22–24].

$$\mathrm{MSE} = \frac{1}{n}\sum_{i=1}^{n}(E_i - P_i)^2, \tag{8}$$

$$\mathrm{MAE} = \frac{1}{n}\sum_{i=1}^{n}|E_i - P_i|. \tag{9}$$

Step 4: The MOGOA is proposed to find the global solutions, in which each grasshopper represents a feasible solution within the design space. The updated position of the i-th solution in the d-th dimension (X_i^d) is computed as:

$$X_i^d = c\left(\sum_{j=1}^{N} c\frac{UD_d - LB_d}{2} s\left(\left|x_j^d - x_i^d\right|\right)\frac{\left|x_j^d - x_i^d\right|}{d_{ij}}\right) + \widehat{T_d}, \quad (10)$$

where UB_d and LB_d present the upper and lower bounds of the dth dimension, respectively, and T_d denotes the best solution identified in that dimension.

The distribution function ($f(x)$) of the Cauchy-Lorentz distribution is expressed as:

$$f(x, x_o, \gamma) = \frac{1}{\pi}\left(\frac{\lambda}{(x - x_o)^2 + \gamma^2}\right), \quad (11)$$

where x_o and γ are the location of the peak of the distribution and the scale parameter, respectively.

The Cauchy-Lorentz distribution-based position (X_i^{CL}) is expressed as:

$$X_i^{CL} = c\left(\sum_{j=1}^{N} c\frac{UD_d - LB_d}{2} s\left(\left|x_j^d - x_i^d\right|\right)\frac{\left|x_j^d - x_i^d\right|}{d_{ij}}\right) + \widehat{T_d} \times \left(1 + \frac{1}{\pi}\left(\frac{\lambda}{(x - x_o)^2 + \gamma^2}\right)\right). \quad (12)$$

The principle of the MOGOA is depicted in Fig. 2.

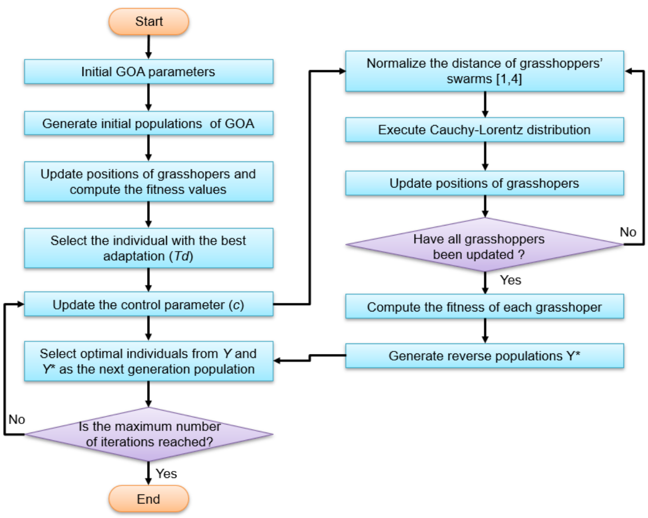

Fig. 2. The working principle of the MOGOA

Step 5: The best point is determined using WASPAS. The total criterion (Q_i) is expressed as:

$$Q_i = \lambda Q_i^{(1)} + (1 - \lambda) Q_i^{(2)}. \quad (13)$$

The highest Q_i is used to select the best optimal point.

3. EXPERIMENTAL SETTING

The AISI H13, extensively used in manufacturing dies and molds, is chosen as the LCMB specimen. The specimen measures 186.0 mm in length, 32.0 mm in width, and 14.0 mm in thickness. The face milling process is used to produce the pre-machined surface, and the *COF* of the initial surface is 0.753.

The burnishing trials are conducted using a CNC milling machine (Fig. 3a). The vibration meter entitled HUATEC HG-5350 is utilized to observe the vibrational amplitude in the X axis. The particle counter is used to measure the $PM10$ over a duration of 20 seconds. The tribometer entitled CETR-UMT2 is applied to measure the *COF* at a constant load of 25 N and a constant sliding time of 1000 s (Fig. 3b).

(a) The burnishing operation

(b) Measuring coefficient of friction and wear depth

Fig. 3. Experimental setting of the burnishing process

The *COF*, *WD*, $PM10$, and *VX* at experimental No. 1 are presented in Fig. 4.

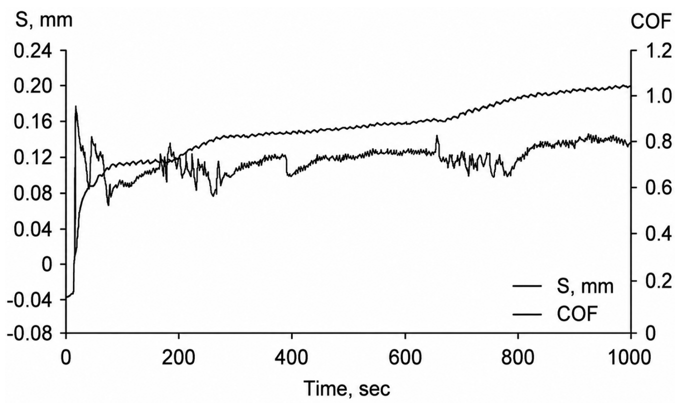

(a) *COF* and *WD* data

Fig. 4

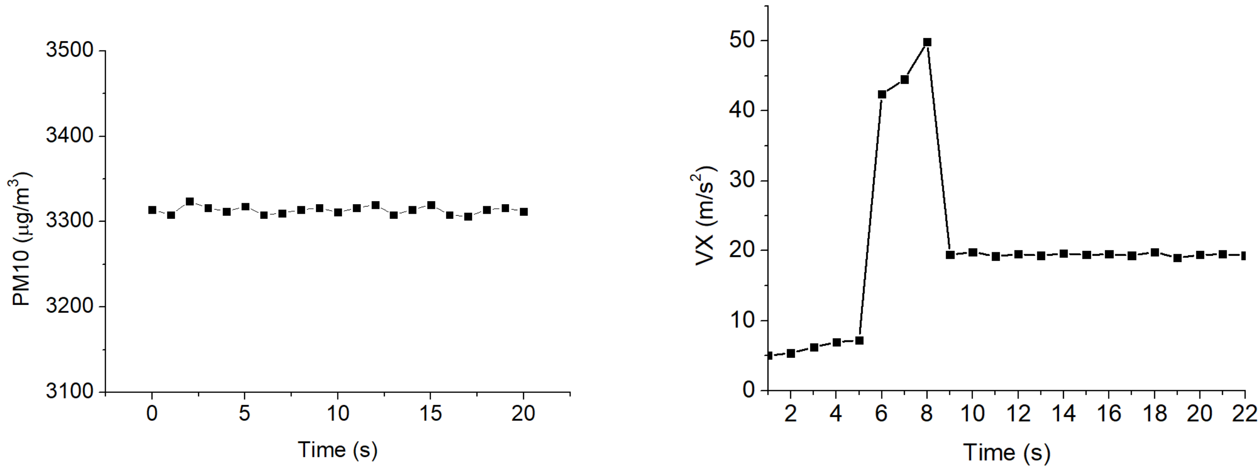

(b) $PM10$ data

(c) VX data

Fig. 4. The LCMB responses at No. 1

4. RESULTS AND DISCUSSION

The LCMB responses are compared at dry, MQL, and LCMQL (CO_2 and MQL) conditions (Fig. 5). It can be stated that the lowest roughness and highest hardness are obtained at the LCMQL. The average roughness in the defined area (*Sa*) values at the LCMQL are reduced from 7.3% to 20.1%, as compared to the MQL one. The *Sa* values at LCMQL are reduced from 19.0% to 35.2% in comparison with the dry condition (Fig. 5a). The friction in the machining region decreases using the MQL and LCMQL, leading to reductions in the roughness. The *VH* values at LCMQL improved from 1.4% to 9.0%, as compared to the MQL one. The *VH* values at LCMQL improved from 4.8% to 9.0%, as compared to the dry one (Fig. 5b). At the dry condition, higher heat is accumulated, leading to the annealing operation; hence, a softer surface is obtained. At the MQL and LCMQL, the heat is significantly removed, leading to the strain hardening behavior; hence, higher *VH* values are achieved.

As shown in Fig. 6, all burnishing conditions produce a plastically deformed surface layer near the top surface, characterized by a refined and densified microstructure compared to the bulk material. The thickness of this affected layer varies significantly depending on the processing condition. Under the LCMQL condition (Fig. 6a), the modified layer is the most uniform and exhibits the greatest depth, indicating a stronger and more stable plastic deformation. In contrast, the MQL condition (Fig. 6b) shows a moderately affected layer with less uniformity, while the dry condition (Fig. 6c) results in the shallowest and most irregular deformation layer. These results demonstrate that the LCMQL approach enhances subsurface microstructural modification more effectively than MQL and dry conditions, which is consistent with the observed improvements in hardness and tribological performance.

The experimental outcomes of the LCMB responses are exhibited in Table 2.

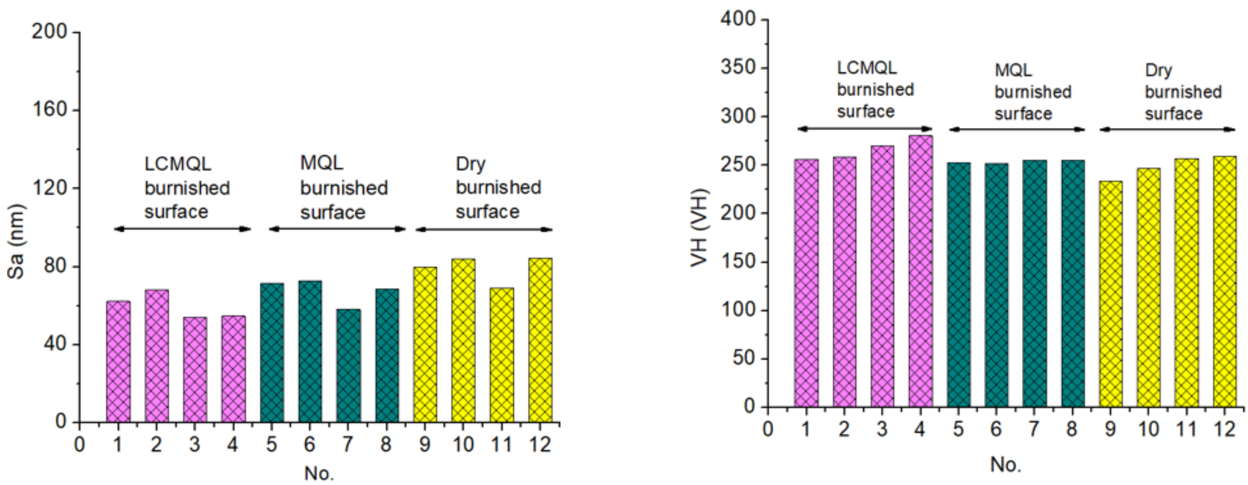

(a) For *Sa* values

(b) For *VH* values

Fig. 5. Comparisons of the Sa and VH values at different burnishing conditions

Table 2
Experimental results of the LCMB operation

No.	*P* (MPa)	*L* (ml/h)	*C* (L/min)	MQL + CO_2				MQL			
				COF	*WD* (mm)	*PM*10 (μg/m^3)	*VX* (m/s^2)	*COF*	*WD* (mm)	*PM*10 (μg/m^3)	*VX* (m/s^2)
Experimental data for developing models											
1	0.2	100	15	0.689	0.181	3314	19.4	0.728	0.189	3201	20.8
2	0.4	100	15	0.681	0.164	9136	16.7	0.719	0.171	8826	17.8
3	0.6	100	15	0.646	0.155	13339	15.3	0.692	0.161	13026	16.5
4	0.2	150	15	0.623	0.162	10538	16.3	0.684	0.168	10265	17.5
5	0.4	150	15	0.605	0.151	13906	13.9	0.638	0.157	13542	14.8
6	0.6	150	15	0.562	0.144	15793	12.8	0.602	0.151	15326	13.6
7	0.2	200	15	0.599	0.149	21656	14.6	0.648	0.156	21163	15.6
8	0.4	200	15	0.572	0.141	22424	12.5	0.615	0.146	22058	13.4
9	0.6	200	15	0.519	0.139	21995	11.7	0.558	0.145	21365	12.5
10	0.2	100	20	0.634	0.169	9655	16.2	0.684	0.175	9365	17.4
11	0.4	100	20	0.618	0.152	15666	13.6	0.648	0.158	15264	14.3
12	0.6	100	20	0.576	0.138	20196	12.1	0.612	0.146	19652	12.9
13	0.2	150	20	0.581	0.149	14273	13.2	0.624	0.156	13946	14.1
14	0.4	150	20	0.555	0.135	17968	10.8	0.594	0.142	17436	11.5
15	0.6	150	20	0.504	0.126	20182	9.6	0.558	0.132	19563	10.3
16	0.2	200	20	0.569	0.136	22638	11.5	0.592	0.142	22046	12.4
17	0.4	200	20	0.534	0.125	24017	9.5	0.572	0.132	23214	10.3
18	0.6	200	20	0.474	0.121	23915	8.6	0.517	0.126	23163	9.4
19	0.2	100	25	0.613	0.165	14992	15.4	0.649	0.172	14536	16.4
20	0.4	100	25	0.589	0.144	21406	12.7	0.629	0.152	20863	13.7
21	0.6	100	25	0.539	0.129	26263	11.2	0.576	0.134	25463	12.2
22	0.2	150	25	0.572	0.145	17218	12.4	0.607	0.151	16842	13.4
23	0.4	150	25	0.539	0.128	21241	10.1	0.576	0.135	20632	10.9
24	0.6	150	25	0.481	0.117	23781	8.8	0.528	0.123	23268	9.4
25	0.2	200	25	0.573	0.131	23115	10.8	0.611	0.138	22463	11.8
26	0.4	200	25	0.531	0.118	24821	8.7	0.568	0.124	24052	9.3
27	0.6	200	25	0.463	0.112	25046	7.8	0.501	0.117	24368	8.4
Experimental data for testing precision of the developed models											
28	0.3	100	17	0.661	0.165	9121	16.4	0.702	0.171	8932	17.5
29	0.5	100	21	0.591	0.141	19361	12.3	0.634	0.149	18945	13.1
30	0.3	150	24	0.558	0.136	18855	11.1	0.598	0.141	18246	11.9
31	0.5	200	19	0.513	0.125	23863	9.3	0.556	0.129	23265	10.1
32	0.3	150	23	0.561	0.137	18265	11.1	0.608	0.142	17842	11.9
33	0.5	200	18	0.521	0.128	23543	9.8	0.564	0.133	23054	10.5
34	0.3	150	20	0.571	0.141	16306	11.8	0.618	0.151	15936	12.6
35	0.5	200	25	0.502	0.113	25119	8.1	0.594	0.118	24452	8.8
36	0.3	150	22	0.562	0.138	17644	11.2	0.606	0.144	17186	11.9
37	0.5	200	16	0.538	0.135	22809	11.6	0.579	0.142	22282	12.3

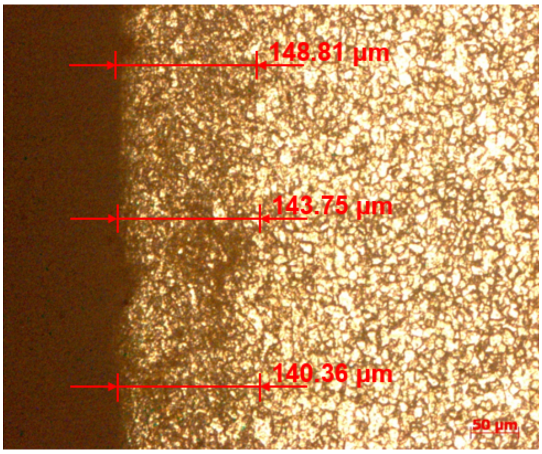

(a) LCMQL

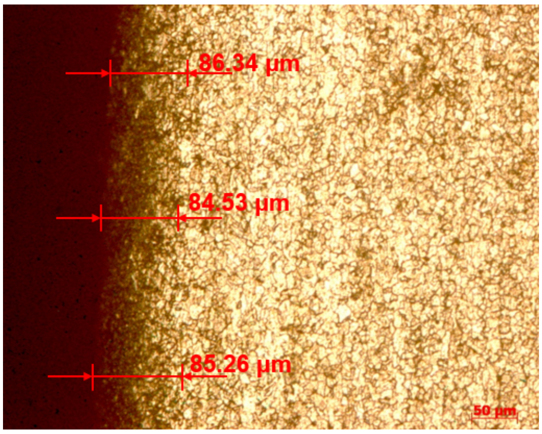

(b) MQL

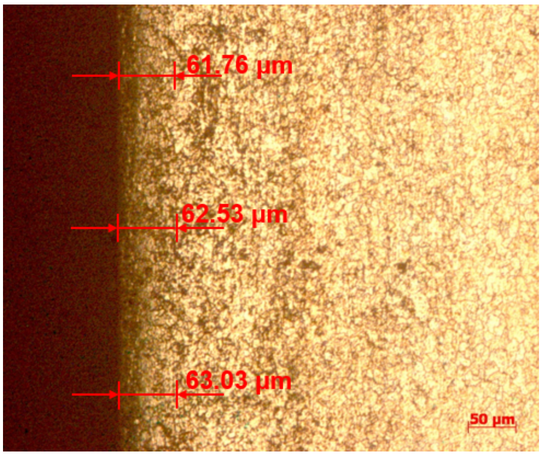

(c) Dry

Fig. 6. The microstructure of the burnished specimens under various conditions

4.1. ANOVA results

The response trends generated from the OSVM predictions were further analyzed using ANOVA [25–28]. All models exhibited high predictive capability with R^2 values above 0.98, while the adjusted and predicted R^2 values were in close agreement, indicating good model reliability and low overfitting tendency (Tables 3–6). Among the investigated parameters, L showed the most noteworthy influence on all responses, followed by the P and C. In addition, several interaction and quadratic terms also exhibited noticeable contributions, demonstrating the coupled effects of cooling and lubrication conditions on the LCMB performance. The ANOVA findings verified that the developed OSVM-based framework can effectively characterize the relationships between cooling parameters and the tribological, environmental, and vibrational responses of the LCMB process. Figures 7a, 7b, 7c, and 7d present the comparisons between the predictive and actual data for COF, WD, $PM10$, and VX, respectively. The uniform distribution of data points indicates that the OSVM models are adequate [29–34].

Table 3
ANOVA results for the *COF* model

So.	SS	MS	F Value	p-value	Cont. (%)
Mo.	0.0388	0.0043	46.65	< 0.0001	
P	0.0076	0.0076	94.50	< 0.0001	19.46
l	0.0083	0.0083	104.02	< 0.0001	21.42
C	0.0067	0.0067	83.82	< 0.0001	17.26
PL	0.0021	0.0021	26.32	0.0028	5.42
PC	0.0016	0.0016	20.01	0.0054	4.12
LC	0.0027	0.0027	33.70	0.0006	6.94
P^2	0.0024	0.0024	30.01	0.0004	6.18
L^2	0.0042	0.0042	52.64	< 0.0001	10.84
C^2	0.0032	0.0032	40.60	< 0.0001	8.36
Res.	0.0006	0.0001			
Cor.	0.0395				
$R^2 = 0.9836$; Adj. $R^2 = 0.9662$; Pred. $R^2 = 0.9516$					

Table 4
ANOVA results for the *WD* model

So.	SS	MS	F Value	p-value	Cont. (%)
Mo.	0.00347	0.000385	128.34	< 0.0001	
P	0.00077	0.000768	255.97	< 0.0001	22.13
L	0.00083	0.000827	275.63	< 0.0001	23.83
C	0.00073	0.000731	243.71	< 0.0001	21.07
PL	0.00027	0.000266	88.72	< 0.0001	7.67
PC	0.00018	0.000185	61.53	< 0.0001	5.32
LC	0.00005	0.000050	16.54	0.0003	1.43
P^2	0.00019	0.000194	64.54	< 0.0001	5.58
L^2	0.00019	0.000185	61.77	< 0.0001	5.34
C^2	0.00026	0.000265	88.25	< 0.0001	7.63
Res.	0.00007	0.000010			
Cor.	0.00353				
$R^2 = 0.9808$; Adj. $R^2 = 0.9616$; Pred. $R^2 = 0.9512$					

Table 5
ANOVA results for the *PM*10 model

So.	SS	MS	F Value	p-value	Cont. (%)
Mo.	3.75E+08	4.17E+07	43.41	< 0.0001	
P	5.72E+07	5.72E+07	66.41	< 0.0001	15.23
L	8.33E+07	8.33E+07	96.58	< 0.0001	22.15
C	7.46E+07	7.46E+07	86.60	< 0.0001	19.86
PL	4.69E+07	4.69E+07	54.42	< 0.0002	12.48
PC	5.11E+06	5.11E+06	5.93	0.0011	1.36
LC	4.98E+07	4.98E+07	57.73	< 0.0001	13.24
P^2	1.44E+07	1.44E+07	16.66	0.0005	3.82
L^2	3.70E+07	3.70E+07	42.91	< 0.0001	9.84
C^2	7.59E+06	7.59E+06	8.81	0.0009	2.02
Res.	6.72E+06	9.61E+05			
Cor.	3.82E+08				
$R^2 = 0.9824$; Adj. $R^2 = 0.9608$; Pred. $R^2 = 0.9502$					

Table 6
ANOVA results for the *VX* model

So.	SS	MS	F Value	p-value	Cont. (%)
Mo.	99.45	11.05	52.62	< 0.0001	
P	20.41	20.41	97.18	< 0.0001	20.52
L	23.56	23.56	112.19	< 0.0001	23.69
C	22.70	22.70	108.12	< 0.0001	22.83
PL	3.49	3.49	16.62	0.0032	3.51
PC	0.43	0.43	2.04	0.7256	0.43
LC	0.57	0.57	2.70	0.6986	0.57
P^2	7.03	7.03	33.48	0.0016	7.07
L^2	8.05	8.05	38.31	0.0007	8.09
C^2	13.22	13.22	62.94	< 0.0001	13.29
Res.	1.49	0.21			
Cor.	100.94				
$R^2 = 0.9852$; Adj. $R^2 = 0.9746$; Pred. $R^2 = 0.9612$					

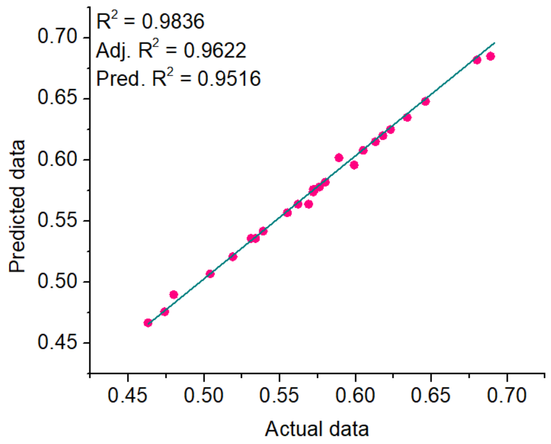

(a) For *COF* model

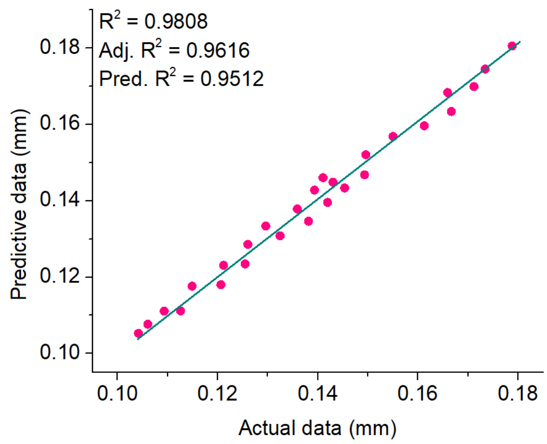

(b) For *WD* model

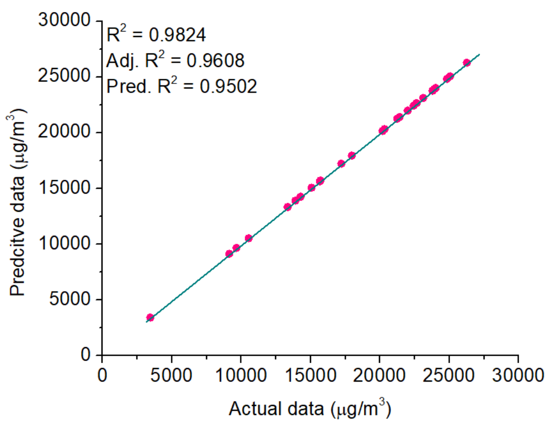

(c) For the *PM*10 model

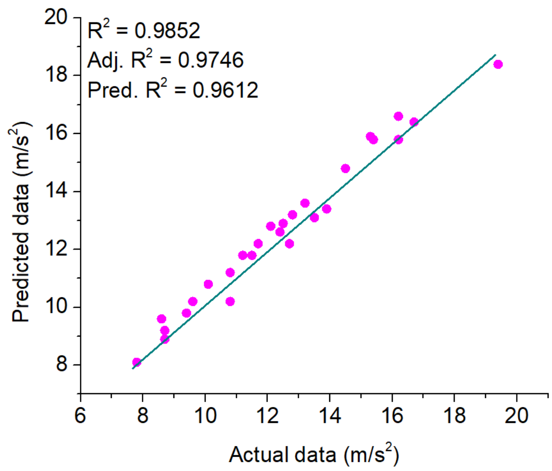

(d) For the *VX* model

Fig. 7. Comparisons between the predicted and actual values for LCMB responses

4.2. Parametric impacts

The combined effects of the cooling parameters on *COF* are illustrated in Fig. 8. The reductions associated with P, L, and C are approximately 7.1%, 14.5%, and 11.5%, respectively. An increase in P leads to finer oil-mist droplets that can more effectively penetrate the contact interface, thereby lowering friction and improving surface smoothness. Similarly, a higher L enhances the amount of lubricant delivered to the interface, facilitating material deformation and reducing surface roughness, which in turn decreases *COF*. In addition, increasing C promotes the formation of a thin lubricating film at the interface, contributing to reduced friction and a smoother surface finish.

The interactive impacts of cooling parameters on the *WD* are depicted in Fig. 9. The relative reductions in terms of the P, L, and C are 16.2%, 18.3%, and 8.9%, respectively. A higher P decreases the machining temperature due to the smaller oil-mist diameter and its higher velocity. A lower machining temperature suppresses thermal softening and promotes strain hardening, resulting in improved surface hardness and reduced *WD*. A higher L increases the lubricant at the interfaces. Plastic deformation is more effectively achieved, resulting in a higher surface hardness; hence, the *WD* decreases. A higher C reduces the resistance due to the generation of a thin film at the burnishing region. The material is smoothly burnished, resulting in a higher surface hardness; hence, a lower *WD* is produced.

The combined influence of the cooling parameters on $PM10$ is presented in Fig. 10. The corresponding increases for P, L, and C are approximately 88.24%, 195.45%, and 108.11%, respectively. Increasing P reduces the oil-mist droplet size while accelerating its velocity, which promotes the generation and dispersion of particulate matter, thereby elevating $PM10$ levels. Likewise, a higher L introduces a greater amount of the lubricant into the air, contributing to increased $PM10$. In addition, raising C enhances the injection of liquid CO_2 into the burnishing zone. The rapid expansion of liquid CO_2 produces a high-momentum turbulent jet, which significantly reduces lubricant droplet size

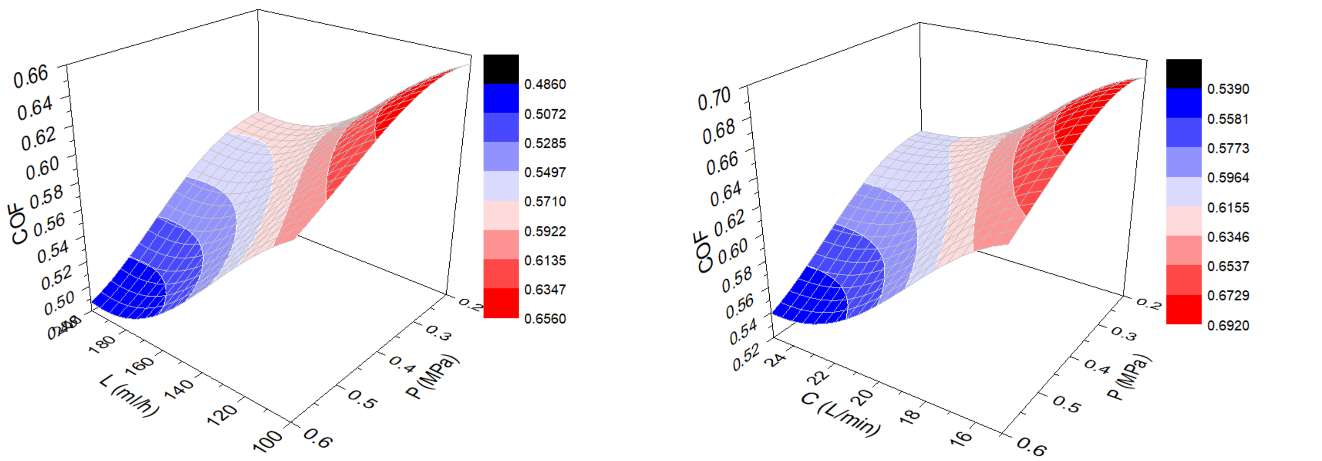

(a) *COF* versus P and L

(b) *COF* versus P and C

Fig. 8. The interactive impacts of cooling parameters on the *COF*

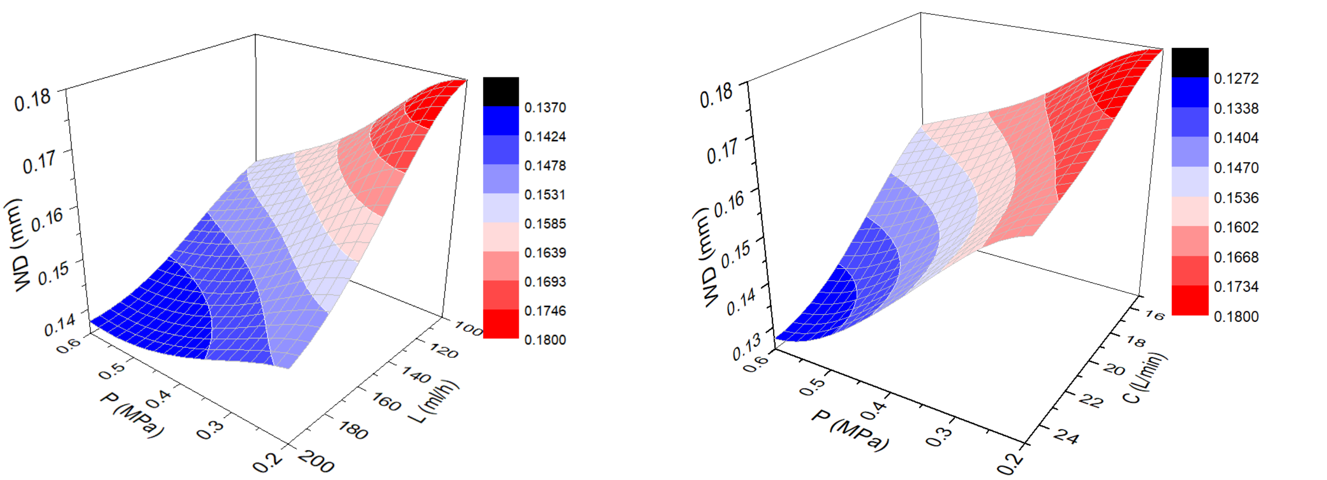

(a) *WD* versus P and L

(b) *WD* versus P and C

Fig. 9. The interactive impacts of cooling parameters on the *WD*

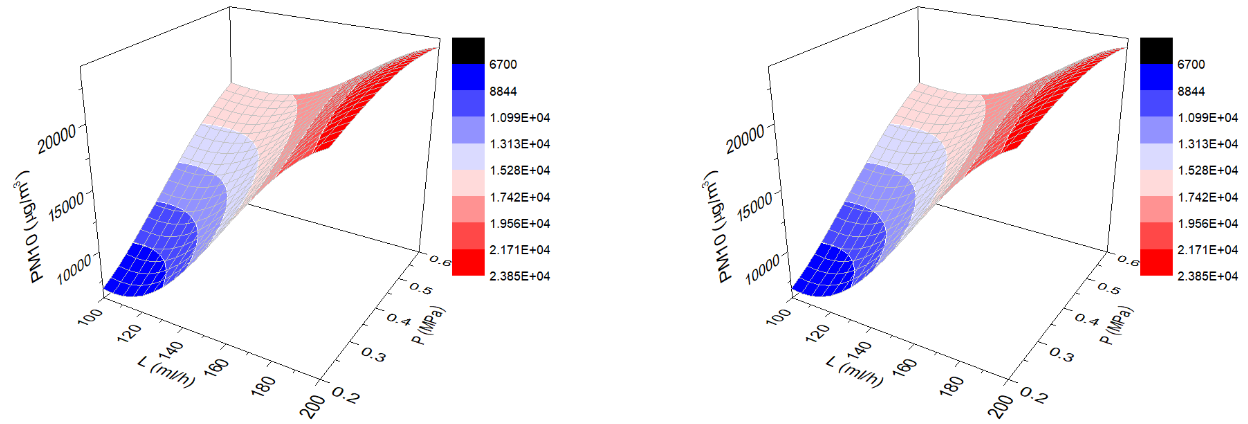

(a) $PM10$ versus P and L

(b) $PM10$ versus P and C

Fig. 10. The interactive impacts of cooling parameters on the $PM10$

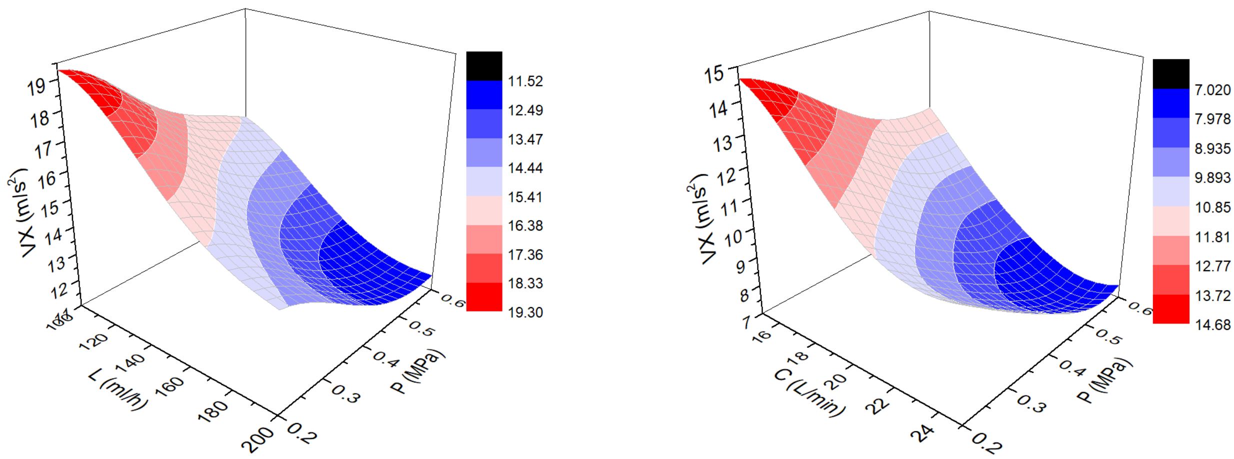

(a) VX versus P and L

(b) VX versus P and C

Fig. 11. The interactive impacts of cooling parameters on the VX

through aerodynamic breakup. Simultaneously, the shear forces at the interface promote the detachment and suspension of wear debris. These combined effects lead to an increase in airborne particles within the $PM10$ size range.

The interactive impacts of cooling parameters on the VX are depicted in Fig. 11. The relative reductions in terms of the P, L, and C are 22.7%, 27.4%, and 21.7%, respectively. A higher P decreases resistance in the machining area, leading to a reduction in the VX. A higher L increases the amount of oil entering the interface region, and the material compression is easily performed; hence, the VX decreases. A higher C produces a thin film at the interfaces, resulting in low friction; hence, the VX is reduced.

4.3. Optimality

The entropy-based weighting analysis assigned relative importance values of 0.22, 0.14, 0.36, and 0.28 to the COF, WD, $PM10$, and VX responses, respectively. The relationships among the LCMB responses are illustrated in Fig. 12, while the optimal solution was selected according to the maximum Q_i value. The obtained optimal cooling conditions corresponded to the P of 0.6 MPa, the L of 150 ml/h, and the C of 17 L/min (Table 7). Under these conditions, the COF, WD, $PM10$, and VX were reduced by 5.9%, 3.5%, 22.3%, and 10.4%, respectively, relative to the predefined target values.

To prove the effectiveness of the MOGOA, the optimal data produced by the NSGA-II are compared. As a result, the optimal P, L, and C are 0.5 MPa, 150 ml/h, and 18 L/min, respectively. The COF, WD, $PM10$, and VX decreased by 4.9%, 2.1%, 21.8%, and 7.2%, respectively, as compared to the user-defined values. It can be stated that MOGOA provides superior optimization performance, as compared to the conventional NSGA-II (Table 7).

The COF of the burnished surface is decreased by 29.3% in comparison with the initial one. The confirmation data of the LCMB responses are presented in Table 8. The deviations from the optimality of the COF, WD, $PM10$, and VX are 1.1%, 1.5%, 0.9%, and 1.8%, respectively, indicating the strength of the obtained findings.

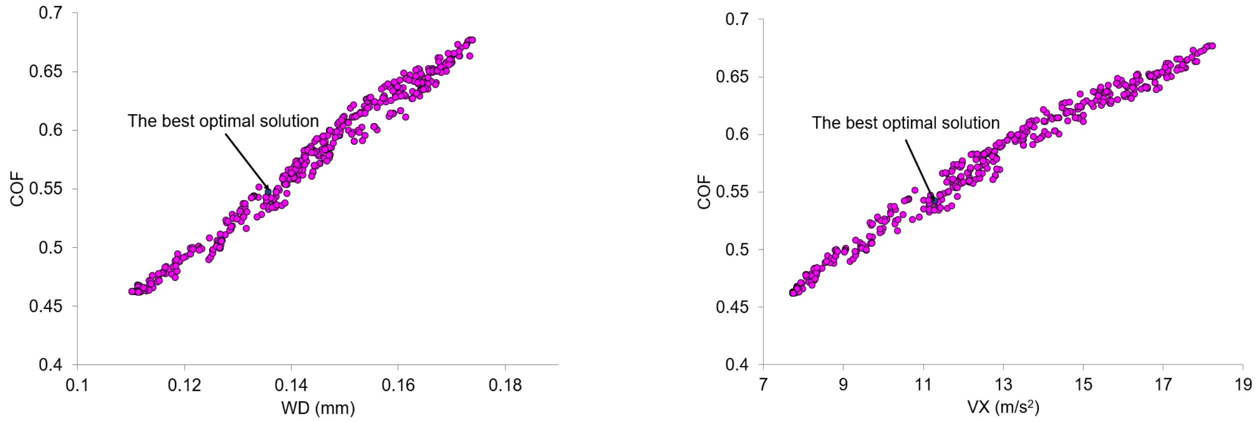

(a) *COF* versus *WD* (b) *COF* versus *VX*

Fig. 12. Pareto fronts produced by the MOGOA

Table 7
Optimization results produced by the MOGOA and NSGA-II

Method	Optimization parameters			Responses				Q_i
	P (MPa)	L (ml/h)	C (L/min)	*COF*	*WD* (mm)	$PM10$ (µg/m^3)	*VX* (m/s^2)	
Initial values	0.4	200	15	0.572	0.141	22424	12.5	
NSGA-II	0.5	150	18	0.544	0.138	17538	11.6	0.6385
Improvement by NSGA-II (%)				−4.9	−2.1	−21.8	−7.2	
MOGOA	0.6	150	17	0.538	0.136	17420	11.2	0.7426
Improvement by MOGOA (%)				−5.9	−3.5	−22.3	−10.4	

Table 8
Confirmation results at the optimality

Method	Optimization parameters			Responses			
	P (MPa)	L (ml/h)	C (L/min)	*COF*	*WD* (mm)	$PM10$ (µg/m^3)	*VX* (m/s^2)
MOGOA	0.6	150	17	0.538	0.136	17420	11.2
Experiment	0.6	150	17	0.532	0.134	17571	11.4
Errors (%)				1.1	1.5	0.9	1.8

5. CONCLUSIONS

An innovative liquid CO_2-MQL burnishing process was successfully developed for improving the tribological and environmental performance of AISI H13 steel. The main findings are summarized as follows:

1. Increasing the cooling-related parameters (P, L, and C) effectively reduced the *COF*, *WD*, and *VX*, while simultaneously increasing $PM10$ due to enhanced lubricant atomization and particle dispersion.
2. The developed OSVM models exhibited excellent predictive capability for all investigated responses, with R^2 values above 0.98 and relative prediction errors below 2.5%.
3. The entropy-MOGOA-WASPAS framework successfully identified the optimal cooling conditions of $P = 0.6$ MPa, $L = 150$ ml/h, and $C = 17$ L/min, under which the *COF*, *WD*, $PM10$, and *VX* were reduced by 5.9%, 3.5%, 22.3%, and 10.4%, respectively.
4. Compared with dry and conventional MQL conditions, the LCMB process produced better surface integrity and subsurface modification, demonstrating its potential for sustainable and intelligent burnishing applications.

ACKNOWLEDGEMENTS

We acknowledge Le Quy Don Technical University, Hanoi, Vietnam, for supporting this study.

We acknowledge Nguyen Tat Thanh University, Ho Chi Minh City, Vietnam, for supporting this study.

Funding

This research is funded by the Vietnam National Foundation for Science and Technology Development (NAFOSTED) under Grant Number NCUD.03-2025.03.

REFERENCES

[1] K.A. Prasad and M.R.S. John, “Optimization of external roller burnishing process on magnesium silicon carbide metal matrix composite using response surface methodology,” *J. Braz. Soc. Mech. Sci. Eng.*, vol. 43, p. 342, 2021, doi: 10.1007/s40430-021-03069-3.

[2] M. Boozarpoor and R. Teimouri, “Parametric study of multi-roller rotary burnishing process,” *Int. J. Lightweight Mater. Manuf.*, vol. 4, pp. 179–194, 2021, doi: 10.1016/j.ijlmm.2020.10.001.

[3] N.T. Varpe and R.S. Tajane, “Parametric optimization for burnishing of AISI-E52100 steel material using multi-objective artificial bee colony algorithm,” *Next Mater.*, vol. 10, p. 101530, 2026, doi: 10.1016/j.nxmate.2025.101530.

[4] H. Hamadache et al., “Full factorial optimization of orthogonal burnishing for enhanced surface properties and wear resistance of XC38 steel,” J. Bio Tribo Corros., vol. 12, p. 67, 2026, doi: 10.1007/s40735-026-01133-w.

[5] G. Rotella, S. Caruso, A. Del Prete, and L. Filice, “Prediction of surface integrity parameters in roller burnishing of Ti6Al4V,” *Metals*, vol. 10, p. 1671, 2020, doi: 10.3390/met10121671.

[6] G. Rotella, S. Rinaldi, and L. Filice, “Roller burnishing of Ti6Al4V under different cooling/lubrication conditions and tool design: Effects on surface integrity,” *Int. J. Adv. Manuf. Technol.*, vol. 106, pp. 431–440, 2020, doi: 10.1007/s00170-019-04631-z.

[7] J. Chen et al., “A study on the optimisation of the fillet roller burnishing process for marine diesel engine crankshafts based on RSM,” *J. Strain Anal. Eng. Des.*, 2026, doi: 10.1177/03093247261418745.

[8] A. Dzierwa, J. Slota, and A. Markopoulos, “Multi-objective optimization of the slide burnishing process for 36CrNiMo4 steel using the TOPSIS approach,” *Adv. Sci. Technol. Res. J.*, vol. 20, no. 3, pp. 387–395, 2026, doi: 10.12913/22998624/214298.

[9] B. Sachin, S. Narendranath, and D. Chakradhar, “Application of desirability approach to optimize the control factors in cryogenic diamond burnishing,” *Arab. J. Sci. Eng.*, vol. 45, pp. 1305–1317, 2020, doi: 10.1007/s13369-019-04326-3.

[10] G.Ü. Başsoy and M. Çelik, “Enhancing surface integrity and wear resistance of DMLS AlSi10Mg via ball burnishing,” *J. Mech. Sci. Technol.*, vol. 40, pp. 609–617, 2026, doi: 10.1007/s12206-025-1251-9.

[11] J. Maximov, G. Duncheva, A. Anchev, V. Dunchev, and Y. Argirov, “Improvement in fatigue strength of chromium-nickel austenitic stainless steels via diamond burnishing and subsequent low-temperature gas nitriding,” *Appl. Sci.*, vol. 14, p. 1020, 2024, doi: 10.3390/app14031020.

[12] B. Sachin, S. Narendranath, and D. Chakradhar, “Enhancement of surface integrity by cryogenic diamond burnishing toward the improved functional performance of the components,” *J. Braz. Soc. Mech. Sci. Eng.*, vol. 41, p. 396, 2019, doi: 10.1007/s40430-019-1918-1.

[13] J. Fan, X. Zhang, N. He, F. Song, and X. Wang, “Investigation on novel deep eutectic solvents with high carbon dioxide adsorption performance,” *J. Environ. Chem. Eng.*, vol. 13, no. 5, p. 117870, 2025, doi: 10.1016/j.jece.2025.117870.

[14] W. Liu, X. Tan, and J. Zhao, “Thermodynamic analysis of cavitation phenomenon in a liquid ammonia injector nozzle,” *Int. Commun. Heat Mass Transf.*, vol. 169, part B, p. 109657, 2025, doi: 10.1016/j.icheatmasstransfer.2025.109657.

[15] C. Lv, Z. Ji, T. Yang, H. Zhao, and H. Zhang, “Numerical simulation of deformation and breakage of compound droplet in air flow,” *Phys. Fluids*, vol. 36, no. 2, p. 023306, 2024, doi: 10.1063/5.0184711.

[16] Z. Zhang, P. Peng, Z. Wang, N. Lin, and Z. Wang, “A charging start time prediction method for electric vehicles based on improved SVM and RF,” *J. Energy Storage*, vol. 152, p. 120457, 2026, doi: 10.1016/j.est.2026.120457.

[17] L. Zhou et al., “Data-driven remaining driving range estimation and analysis framework for electric vehicles under real-world conditions,” *Appl. Energy*, vol. 402, Part B, p. 126881, 2026, doi: 10.1016/j.apenergy.2025.126881.

[18] Y. Özüpak, “Machine learning-based fault detection in transmission lines: A comparative study with random search optimization,” *Bull. Polish Acad. Sci. Tech. Sci.*, vol. 73, no. 2, p. e153229, 2025, doi: 10.24425/bpasts.2025.153229.

[19] M. Çınar, E. Aslan, and Y. Özüpak, “Comparison and optimization of machine learning methods for fault detection in district heating and cooling systems,” *Bull. Polish Acad. Sci. Tech. Sci.*, vol. 73, no. 3, p. e154063, 2025, doi: 10.24425/bpasts.2025.154063.

[20] M. Mungan and O. Arpa, “Estimation of CO_2 emissions from vehicles using machine learning and multi-model investigation,” *Bull. Polish Acad. Sci. Tech. Sci.*, vol. 73, no. 4, p. e154287, 2025, doi: 10.24425/bpasts.2025.154287.

[21] J. He, J. Wu, J. Ni, Y. Zhang, and K. Siau, “Real-time task scheduling strategy for 3D printing cloud platforms in health scenes,” *Appl. Intell.*, vol. 55, no. 15, pp. 1–17, 2025, doi: 10.1007/s10489-025-06907-2.

[22] L. He, W. Gong, and J. Zhao, “Research on fuel injection quantity fluctuation characteristics and optimization improvement of dual-fuel engines,” *Energy*, vol. 324, no. 2, p. 135953, 2025, doi: 10.1016/j.energy.2025.135953.

[23] J. Xu, D. Xu, H. Lu, J. Yang, W. Mahfoudi, and J. Lian, “Research on the shape-dependence of nano-copper and the friction and lubrication mechanisms under the synergistic effect of multiple shapes,” *Tribol. Int.*, vol. 219, p. 111832, 2026, doi: 10.1016/j.triboint.2026.111832.

[24] Z. Ni *et al.*, “Enhanced formation quality and mechanical properties of ultrasonic spot welding of TA2 Ti sheets by pure Al coating,” *J. Mater. Process. Technol.*, vol. 156, Part A, pp. 1–16, 2025, doi: 10.1016/j.jmapro.2025.10.084.

[25] Z. Ling, S. Li, J. Liu, W. Chen, and Z. Fu, “Critical Nb induced interfacial armoring for enhanced molten Al tribo-corrosion resistance in Ti–Nb–Cr refractory alloys,” *Wear*, vol. 584–585, p. 206439, 2025, doi: 10.1016/j.wear.2025.206439.

[26] Y. Liu, J. Dong, S. Yuan, J. Yu, Z. Guan, H.K. Chai, and Q. Wang, “Impact resistance and enhancing mechanism of a novel mortar integrated with shear thickening fluid,” *Constr. Build. Mater.*, vol. 498, p. 144036, 2024, doi: 10.1016/j.conbuildmat.2025.144036.

[27] Z. Zhao, L. Sun, X. Zhao, and Y. Liu, “Modeling and dynamics analysis of a rigid–flexible coupled satellite,” *Aerosp. Sci. Technol.*, vol. 156, p. 116808, 2026, doi: 10.1016/j.ast.2026.116808.

[28] Z. Ling, W. Yang, W. Chen, and Z. Fu, “Recent advances in understanding the corrosive effects of molten aluminum on structural materials and protective strategies: A comprehensive review,” *Mater. Today Commun.*, vol. 47, p. 113249, 2025, doi: 10.1016/j.mtcomm.2025.113249.

[29] D. Li et al., “Battery thermal runaway fault prognosis in electric vehicles based on abnormal heat generation and deep learning algorithms,” IEEE Trans. Power Electron., vol. 37, no. 7, pp. 8513–8525, 2022, doi: 10.1109/TPEL.2022.3150026.

[30] Z. Zhang, S. Sun, Z. Wang, and N. Lin, “Battery retirement state prediction method based on real-world data and the TabNet model,” *Energy*, vol. 334, p. 137795, 2025, doi: 10.1016/j.energy.2025.137795.

[31] N. Lin, K. Chen, Z. Zhang, S. Chen, and Z. Wang, “Beyond diagnosis: Why current fault diagnosis methods for power batteries fall short,” *J. Energy Storage*, vol. 130, p. 117225, 2025, doi: 10.1016/j.est.2025.117225.

[32] A. Rojas, M.A. Gómez, and J.H. Arango, “Quasi-symplectic ADRC hybridization to stabilize a flexible truss structure for space telescopes,” *Aerosp. Sci. Technol.*, vol. 164, p. 110760, 2026, doi: 10.1016/j.ast.2026.110760.

[33] K. Piasta and R. Trębiński, “Projectile shape optimization using numerical twin with computational fluid dynamics and design of experiment methods,” *Bull. Pol. Acad. Sci. Tech. Sci.*, vol. 74, no. 2, p. e157329, 2026, doi: 10.24425/bpasts.2026.157329.

[34] S. Gladson and K. Pandiarajan, “DODGE: Congestion control in MANET via dragonfly optimized deep learning model,” *Bull. Pol. Acad. Sci. Tech. Sci.*, vol. 73, no. 3, p. e153231, 2025, doi: 10.24425/bpasts.2025.153231.